AUT Journal of Modeling and Simulation

AUT J. Model. Simul., 58(1) (2026) 95-112
DOI: 10.22060/miscj.2026.24965.5445

Transient Natural Convection and Thermal Performance Analysis in Stratified Water-Filled Rectangular and Square Cavities: A Comparative Study

Md. Nayem Hossain[1], Syed Mehedi Hassan Shaon[1], Md. Mahafujur Rahaman[2,3] *

[1] Department of Chemical Engineering, Z. H. Sikder University of Science and Technology, Shariatpur 8024, Bangladesh.
[2] Department of Computer Science and Engineering, Z. H. Sikder University of Science and Technology, Shariatpur 8024, Bangladesh.
[3] Department of Mathematics, Jagannath University, Dhaka 1100, Bangladesh.

ABSTRACT: This study numerically analyzes transient natural convection (NC), heat transfer (HT), and entropy generation (Egen) in a thermally stratified rectangular enclosure and compares its thermal performance with that of a square enclosure filled with stratified water. Both enclosures are heated from the bottom, cooled from the top, and bounded by thermally stratified vertical walls. The governing equations are solved utilizing the finite volume (FV) scheme for a Prandtl number (Pr) of 7.01 over a Rayleigh number (Ra) range from 10 to 107. The evolution of flow and thermal characteristics is analyzed through isotherms, streamlines, temperature time series (TTS), phase-space trajectories, average Nusselt number (Nuavg), average entropy generation (Eavg), average Bejan number (Beavg), and ecological coefficient of performance (ECOP). The findings show that increasing Ra drives the flow through successive transitions from steady symmetric to asymmetric, periodic, and ultimately chaotic states. In the rectangular enclosure, three critical bifurcations are identified: a pitchfork bifurcation between Ra = 2×10^4 and 3×10^4, a Hopf bifurcation between Ra = 10^5 and 2×10^5, and a shift from periodic to chaotic flow between Ra = 5×10^6 and 7 × 106. Quantitative analysis further shows that the square enclosure provides a higher Nuavg over most of the investigated range ($10 < Ra \leq 10^6$). However, at Ra = 7×10^6, the rectangular enclosure achieves a 7.21% higher Nuavg and an approximately 6.3% higher ECOP than the square enclosure, indicating superior HT capability and thermodynamic efficiency under highly convective conditions.

Review History:

Received: Oct. 22, 2025
Revised: Jul. 15, 2026
Accepted: Jul. 18, 2026
Available Online: Jul. 20, 2026

Keywords:

Transient Flow
Natural Convection
Bifurcations
Entropy Generation
Heat Transfer

1- Introduction

Natural convection (NC) inside enclosed cavities has attracted considerable attention owing to its fundamental importance in a wide range of engineering applications, including building insulation, electronic cooling, solar thermal collectors, heat exchangers, and thermal energy storage systems (Bergman [1]; Bejan [2]). Buoyancy-driven flow induced by temperature gradients between heated and cooled boundaries gives rise to complex flow and heat transfer (HT) characteristics that are powerfully influenced by cavity geometry, thermal boundary conditions, and fluid properties. Consequently, understanding the transport mechanisms governing NC in enclosed domains is crucial for improving the thermal transport and energy effectiveness of numerous engineering systems. Over the years, extensive numerical, experimental, and analytical studies have been conducted on NC in square, rectangular, trapezoidal, and cylindrical enclosures subjected to various thermal and physical conditions. In addition to conventional enclosure studies, several researchers have examined more complex transport phenomena involving magnetic fields, rotation, porous media, and non-Newtonian fluids. For example, Rahman et al. [3] investigated magnetohydrodynamic (MHD) NC heat and mass transfer over a perpendicular porous plate in a revolving system with a stimulated magnetic field. Their results illustrated that snowballing either the magnetic field strength or the rotation parameter suppresses fluid velocity through the Lorentz force while significantly altering the thermal boundary layers, thereby emphasizing the critical impact of the induced magnetic field on coupled heat and mass transport processes. Likewise, Kawser and Rahaman [4] obtained exact travelling-wave solutions for the Jeffery-Hamel flow of a non-Newtonian fluid utilizing the sine-cosine method. Their analytical study revealed that both the velocity distribution and flow characteristics are highly sensitive to fluid rheology and geometric parameters, while also confirming the effectiveness of the proposed analytical approach in describing nonlinear flow behavior.

Thermally stratified fluids, characterized by variations in density due to temperature gradients, play a critical role in NC

*Corresponding author's email: Email

and HT phenomena. Thermal stratification can significantly influence flow patterns, suppress or enhance convective motion, and modify HT rates within confined enclosures (Zoubir et al. [5]). In industrial applications including solar energy storage, electronic cooling, and building ventilation, understanding stratification effects is indispensable for optimizing thermal performance and energy efficiency. Recent studies have also focused on the transient behavior of buoyancy-driven flows in thermally stratified enclosures, where the initial temperature distribution is crucial in determining the evolution of fluid motion and HT. Rahaman et al. [6] investigated unsteady convective HT in a thermally stratified air-filled enclosure subjected to uniform cooling at the upper wall. Subsequently, Rahaman et al. [7] examined unsteady NC of the same cavity configuration introduced in [6]. Their study showed that the initial thermal stratification markedly affects the emergence and development of buoyancy-driven circulation, leading to substantial changes in flow structures and temperature distributions. Moreover, stronger thermal stratification was found to delay the initiation of convection and suppress HT, highlighting the significant role of stratification in governing unsteady convective transport within enclosed domains. Extending this line of research, Rahaman et al. [8] numerically investigated unsteady NC and HT in a stratified trapezoidal enclosure and further confirmed that the intensity of thermal stratification has a pronounced impact on HT performance.

A comprehensive understanding of NC in cavities with diverse geometrical arrangements, including square, rectangular, trapezoidal, cylindrical, and other cavity shapes, is essential for advancing thermal system design and performance optimization. The geometry of the enclosure has a profound impact on buoyancy-induced flow behavior, temperature circulation, and overall HT characteristics. Changes in enclosure shape alter the development of thermal and hydrodynamic boundary layers, modify flow patterns, and affect the emergence of flow instabilities, thereby governing the effectiveness of HT and the thermal performance of enclosed systems. Bouafia and Daube [9] explored NC around a square solid obstacle enclosed within a rectangular enclosure under large temperature gradients. Their study demonstrated that pronounced thermal gradients substantially modify the flow structure and promote enhanced HT in the neighborhood of the solid body. Rahaman et al. [10] studied NC within a V-shaped enclosure encompassing two-phase fluids and demonstrated that increasing the Ra induces a shift from steady to chaotic flow in the air phase, whereas no such changeover occurs in the water phase. Karatas and Derbentli [11] studied NC in non-uniformly heated rectangular cavities under time-periodic thermal boundary conditions and reported that periodic wall temperature oscillations substantially modify the fluid flow and temperature distribution, giving rise to oscillatory convective behavior. Charles et al. [12] studied turbulent NC inside a rectangular enclosure and demonstrated that turbulence significantly augments HT compared with laminar flow while producing highly transient and complex temperature and velocity fields. Berdnikov et al. [13] investigated the transient expansion of NC following the abrupt heating of a side wall in a rectangular enclosure. Their results showed that abrupt thermal irritation generates rapidly evolving flow patterns and temperature fields, leading to intricate transient circulation structures. In an analytical study, Fichera et al. [14] advanced a theoretical model for NC in a rectangular enclosure with non-uniformly heated side walls and demonstrated that the imposed wall temperature difference strongly governs the formation of circulation cells and thermal boundary layers (TBL). More recently, Farahani et al. [15] explored NC inside a tall rectangular enclosure encompassing an oscillating and revolving cylinder. Their findings revealed that the cylinder's oscillatory and rotational motions substantially modify the flow structure and thermal field. Begum et al. [16] numerically investigated NC in rectangular cavities considering viscous dissipation and interior heat production for diverse aspect ratios.

Square enclosures have been widely adopted as canonical configurations for investigating NC because of their simple geometry and well-defined thermal boundary conditions. These characteristics make them ideal benchmark models for exploring fundamental thermo-fluid phenomena, including boundary layer formation, flow instability, and the changeover from laminar to turbulent convection. Consequently, many numerical, analytical, and experimental studies have employed square cavities to enhance the understanding of buoyancy-driven transport mechanisms. Among the pioneering investigations, De Vahl Davis [17] established a benchmark numerical solution for NC in a square cavity, providing highly accurate steady-state results over the Ra range of 10^3 to 10^6. Pesso and Piva [18] subsequently extended this work to low Pr fluids with significant density gradients, demonstrating the constraints of the Boussinesq approximation and providing a more realistic description of thermally driven flow. Hakeem et al. [19] examined NC in a square enclosure containing thermally active plates under various thermal boundary conditions and showed that both the location and temperature of the plates strongly influence the flow field and HT performance. Choi and Kim [20] performed a comparative assessment of several thermal lattice Boltzmann models for computing NC in square cavities, evaluating their numerical stability and predictive capability over a wide variety of Ra. Butler et al. [21] experimentally investigated NC from a heated horizontal cylinder placed inside a square cavity and demonstrated that the collaboration between the cylinder and the enclosure walls suggestively alters the circulation patterns and augments local HT. More recently, Saravanan [22] numerically studied NC within a square enclosure equipped with internally heat-generating baffles, revealing that the baffle dimensions, placement, and heat generation intensity substantially affect the flow characteristics and HT in the cavity.

Direct numerical and experimental studies on NC in square cavities have provided extensive insights into flow structures, thermal behavior, and HT mechanisms under various configurations. Kouroudis et al. [23] performed direct numerical simulations with uniform heat fluxes on the perpendicular walls, revealing the development of multiple circulation cells and the changeover from steady to transient flow with increasing Ra, along with critical thresholds for the onset of oscillatory convection. El Moutaouakil et al. [24] examined NC in conjunction with surface radiation in a square enclosure containing an inner wavy body, showing that cavity inclination, wavy geometry, and radiative effects meaningfully affect flow patterns and temperature distributions. Wang et al. [25] analyzed unsteady NC within a square cavity with a centrally heated circular cylinder, demonstrating that the cylinder's vertical position markedly affects the onset and intensity of periodic flow and thermal oscillations, thereby modifying overall HT performance. Oyewola et al. [26] investigated convective HT in a square cavity with a circular embedded heat source, highlighting that block location strongly governs circulation patterns, temperature fields, and HT efficiency. El and Lafdaili [27] studied turbulent NC within a nanofluid-filled square enclosure under an applied magnetic field, revealing that nanoparticle concentration, Ra, and magnetic field orientation collectively influence flow structures and thermal transport. Zemani et al. [28] explored NC in a square enclosure with a partially heated curved wall, demonstrating that wall geometry and heating configuration strongly determine flow organization and HT performance. Bawazeer and Alsoufi [29] examined the effects of Pr and Ra, showing that higher Ra intensifies buoyancy-driven circulation and thermal gradients, while variations in Pr significantly affect thermal and velocity boundary layer development.

Entropy generation (E_{gen}) investigation has been used as a vital tool for measuring the thermodynamic performance of convective HT systems, quantifying energy losses in accordance with the second law of thermodynamics, and guiding strategies for efficiency improvement. Shavik et al. [30] explored NC and E_{gen} inside a tilted square cavity, reporting that total E_{gen} increased and the Bejan number (*Be*) decreased with rising Ra, while increasing the inclination angle enhanced E_{gen} due to fluid friction but reduced both total E_{gen} and *Be*. Ilis et al. [31] performed numerical simulations of E_{gen} in rectangular enclosures with varying aspect ratios, demonstrating significant variations in total E_{gen} and local *Be* distributions. Shuja et al. [32] analyzed conductive HT and E_{gen} in a square enclosure containing a heat-generating body, examining the impacts of its positional variations on entropy production. Hussein et al. [33] carried out a numerical study of three-dimensional NC and E_{gen} in leaning cubical trapezoidal air-filled enclosures, illustrating the contribution of both HT and fluid friction to energy losses. Rahaman et al. [34] extended this analysis to unsteady NC in trapezoidal cavities, showing that higher Ra enhances E_{gen} while decreasing energy efficiency. Charreh et al. [35] numerically studied MHD NC and E_{gen} in a porous square enclosure with four integrated cylinders, showing that magnetic field strength and cylinder arrangement strongly influence fluid flow, HT, and E_{gen}, with higher magnetic intensity suppressing convection and reducing entropy. Rahaman et al. [36] investigated unsteady NC and E_{gen} in a trapezoid-shaped enclosure, focusing on the influence of Ra on thermal performance. Recently, Rahaman et al. [37] performed a comparative study of air- and water-filled trapezoidal enclosures, finding that air-filled cavities exhibited higher average HT, whereas water-filled cavities produced greater average E_{gen}. More recently, Hossain et al. [38] conducted a numerical study on transient NC and E_{gen} in a stratified square enclosure. Their investigation studied the influence of thermal stratification, Ra, and fluid properties on flow evolution, temperature distribution, and entropy production.

Although NC in rectangular and square enclosures has been extensively investigated, the combined influence of a uniformly heated bottom wall, a uniformly cooled top wall, and thermally stratified vertical walls in water-filled enclosures has received comparatively limited attention. In particular, studies addressing the transient evolution of buoyancy-driven flow, bifurcation behavior, and thermodynamic irreversibility under these thermal boundary conditions remain scarce. Furthermore, a comprehensive comparison of the thermal performance of rectangular and square enclosures containing thermally stratified water has yet to be systematically reported. To address this research gap, the current study conducts a comparative numerical investigation of NC in rectangular and square enclosures occupied with stratified water. The two cavity configurations are designed to have identical surface areas, with differences arising solely from their length-to-width ratios. The key objective is to investigate the impact of the Ra on flow evolution, HT, and E_{gen}, with a specific focus on determining the critical Ra correlated with pitchfork bifurcation, Hopf bifurcation, and the transition to chaotic flow in the rectangular enclosure. Moreover, the thermal and thermodynamic performances of the square and rectangular enclosures are systematically compared to evaluate the influence of cavity geometry on buoyancy-driven transport. The numerical model is finally validated against well-established benchmark solutions accessible in the literature to confirm the accuracy and reliability of the predicted outcomes.

2- Methodology

In this study, at first two-dimensional NC and E_{gen} within a rectangular cavity are first investigated under the prescribed boundary conditions, as illustrated in the schematic diagram depicted in Fig. 1. This study focuses on two-dimensional numerical simulations, aimed at understanding the dynamics of unsteady NC, HT, and E_{gen} in a rectangular enclosure. Then, a comparative assessment of thermal performance between rectangular and square geometries is subsequently conducted. The bottom wall is maintained at a uniformly high temperature, denoted as T_h; the top wall is kept at a comparatively lower temperature, T_c. The vertical sidewalls are characterized by a linear thermal gradient, labeled T_i. The cavity is filled with a fluid having a Pr of 7.01, representing initially thermally stratified water. The corresponding thermophysical properties of the stratified water are summarized in Table 1. The comparative study was conducted between the present rectangular cavity and

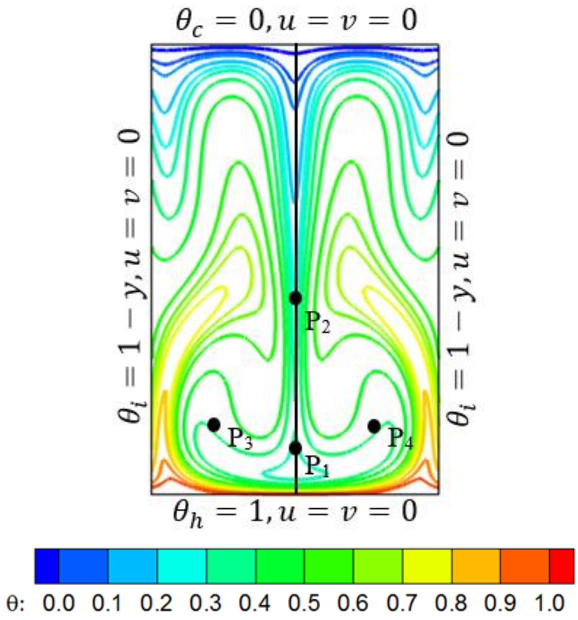

Fig. 1. Physical domain and dimensionless boundary conditions; results monitoring points P_1 (0, 0.15), P_2 (0, 0.40), P_3 (-0.30, 0.20), and P_4 (0.30, 0.20) employed in the subsequent figures.

the authors' previous investigation [38]. In this comparison, the surface areas and boundary conditions were identical for both the square cavity [38] and the present rectangular cavity, with variations applied only to their length and height. All boundaries are supposed to be fixed and subject to non-slip conditions.

Using a two-dimensional model, the behavior of stratified water under NC is investigated within rectangular and square enclosures. The governing equations based on the Boussinesq-approximated Navier-Stokes and energy formulations (refer to [8]) are as follows:

$$\frac{\partial U}{\partial X}+\frac{\partial V}{\partial Y}=0, \tag{1}$$

$$\frac{\partial U}{\partial t}+U\frac{\partial U}{\partial X}+V\frac{\partial U}{\partial Y}=-\frac{1}{\rho}\frac{\partial P}{\partial X}+\nu\left(\frac{\partial^2 U}{\partial X^2}+\frac{\partial^2 U}{\partial Y^2}\right), \tag{2}$$

$$\frac{\partial V}{\partial t}+U\frac{\partial V}{\partial X}+V\frac{\partial V}{\partial Y}=-\frac{1}{\rho}\frac{\partial P}{\partial Y}+\nu\left(\frac{\partial^2 V}{\partial X^2}+\frac{\partial^2 V}{\partial Y^2}\right)+g\beta\left(T-T_0\right), \tag{3}$$

$$\frac{\partial T}{\partial t}+U\frac{\partial T}{\partial X}+V\frac{\partial T}{\partial Y}=\alpha\left(\frac{\partial^2 T}{\partial X^2}+\frac{\partial^2 T}{\partial Y^2}\right). \tag{4}$$

The dimensional boundary condition is as follows:

$$\begin{cases}\text{Top cold wall: } T=T_c, U=V=0,\\ \text{Bottom heated wall: } T=T_h, U=V=0,\\ \text{Vertical stratified walls: } T=T_i, U=V=0.\end{cases} \tag{5}$$

The following are the dimensionless variables that were employed:

$$x=\frac{X}{Y}, y=\frac{Y}{H}, u=\frac{UH}{\alpha\sqrt{\text{Ra}}}, v=\frac{VH}{\alpha\sqrt{\text{Ra}}},$$
$$p=\frac{PH^2}{\rho\alpha^2\text{Ra}}, \theta=\frac{T-T_\infty}{T_h-T_c}, \tau=\frac{t\alpha\sqrt{\text{Ra}}}{H^2}. \tag{6}$$

Two governing parameters, Pr and Ra, are defined as:

$$\text{Pr}=\frac{\nu}{\alpha} \text{ and } \text{Ra}=\frac{g\beta\left(T_h-T_c\right)H^3}{\nu\alpha}. \tag{7}$$

The dimensionless form of Eqs. (1) to (4) becomes [38]:

$$\frac{\partial u}{\partial x}+\frac{\partial v}{\partial y}=0, \tag{8}$$

$$\frac{\partial u}{\partial \tau}+u\frac{\partial u}{\partial x}+v\frac{\partial u}{\partial y}=-\frac{\partial p}{\partial x}+\frac{\Pr}{\sqrt{\mathrm{Ra}}}\left(\frac{\partial^2 u}{\partial x^2}+\frac{\partial^2 u}{\partial y^2}\right), \tag{9}$$

$$\frac{\partial v}{\partial \tau}+u\frac{\partial v}{\partial x}+v\frac{\partial v}{\partial y}=-\frac{\partial p}{\partial y}+\frac{\Pr}{\sqrt{\mathrm{Ra}}}\left(\frac{\partial^2 v}{\partial x^2}+\frac{\partial^2 v}{\partial y^2}\right)+\Pr\theta, \tag{10}$$

$$\frac{\partial \theta}{\partial \tau}+u\frac{\partial \theta}{\partial x}+v\frac{\partial \theta}{\partial y}=\frac{1}{\sqrt{\mathrm{Ra}}}\left(\frac{\partial^2 \theta}{\partial x^2}+\frac{\partial^2 \theta}{\partial y^2}\right). \tag{11}$$

where *u, v, x, y, p,* τ, and *θ* represent the dimensionless forms of *U, V, X, Y, P, t,* and *T*, respectively.

The dimensionless boundary conditions are as follows:

$$\begin{cases}\theta_c = u = v = 0, \text{at the top wall}\\ \theta_h = 1,\ u = v = 0, \text{at the bottom wall}\\ \theta_i = 1-y,\ u = v = 0, \text{at the vertical walls.}\end{cases} \tag{12}$$

The average Nusselt number along the horizontal and vertical walls, denoted as $[Nu_{avg}]_h$ and $[Nu_{avg}]_v$, respectively, are defined as follows [38, 39]:

$$\left[Nu_{avg}\right]_h=\frac{1}{l}\int_0^1\frac{\partial\theta}{\partial y}dx \,\text{and}\left[Nu_{avg}\right]_v=\frac{1}{l}\int_0^1\frac{\partial\theta}{\partial x}dy. \tag{13}$$

Thermodynamic irreversibility in an NC system arises primarily from HT and FF. Based on linear transport theory (see Shavik et al. [31]), the normalized local E_{gen} for these mechanisms can be formulated as:

$$E_{ht}=\left(\frac{\partial\theta}{\partial x}\right)^2+\left(\frac{\partial\theta}{\partial y}\right)^2, \tag{14}$$

$$E_{ff}=\psi\left[2\left\{\left(\frac{\partial u}{\partial x}\right)^2+\left(\frac{\partial v}{\partial y}\right)^2\right\}+\left(\frac{\partial u}{\partial y}+\frac{\partial v}{\partial x}\right)^2\right]. \tag{15}$$

where E_{ht} and E_{ff} represent the local E_{gen} due to HT and FF, respectively. In Eq. (15), ψ denotes the irreversibility distribution ratio, which is defined as:

$$\psi=\frac{\mu T_\infty}{\alpha}\left(\frac{k}{L\Delta T}\right)^2. \tag{16}$$

The local E_{gen} inside the cavity, denoted as E_l, obtained by adding Eqs. (14) and (15) is defined as [34]:

$$E_l=E_{ht}+E_{ff}. \tag{17}$$

The local Bejan number (Be_l), average Bejan number (Be_{avg}), and average entropy generation (E_{avg}) are defined as follows [30]:

$$Be_l=\frac{E_{ht}}{E_{ht}+E_{ff}}. \tag{18}$$

$$Be_{avg}=\frac{\int_0^1\int_0^1 Be_l\,dx\,dy}{\int_0^1\int_0^1 dx\,dy}. \tag{19}$$

$$E_{avg}=\frac{\int_0^1\int_0^1 E_l\,dx\,dy}{\int_0^1\int_0^1 dx\,dy}. \tag{20}$$

3- Numerical Model

The governing equations Eqs. (8)-(11), together with the boundary conditions defined in Eq. (12), were solved numerically utilizing the finite volume (FV) method implemented in ANSYS Fluent 17.0 (refer to [36, 37]). Pressure-velocity coupling was handled using the Semi-Implicit Method for Pressure-Linked Equations (SIMPLE) algorithm. The viscous diffusion terms were discretized employing a second-order central differencing scheme, whereas the convective terms were approximated using the third-order Quadratic Upstream Interpolation for Convective Kinematics (QUICK) scheme to achieve improved numerical accuracy [40]. A non-uniform structured rectangular mesh was employed to augment spatial resolution, particularly in regions with steep velocity and temperature gradients. In addition, appropriate under-relaxation factors were incorporated to improve the stability and convergence of the iterative solution procedure, following the methodology described by Rahaman et al. [37, 38]. For transient simulations, the temporal derivatives were discretized applying a second-order implicit time-integration scheme, providing enhanced temporal precision and numerical stability. A convergence threshold of 10^{-5} is applied to the governing equations for energy, momentum, and continuity.

Table 1. Thermophysical properties of the working fluid (refer to [30]).

Property (unit)	Stratified fluid (water)
ρ (kg/m^3)	998.4
C_p (J/kg K)	4182
μ (kg/m s)	0.0009475
k (W/m K)	0.566

4- Grid and Time Step Dependent Tests

The grid resolution within the computational domain plays a crucial role in determining the accuracy and reliability of the numerical results. To assess the effects of grid resolution and time-step size, a grid sensitivity analysis was carried out at Ra = 10^7. The study employed time steps of 0.01 and 0.005, and grid refinement tests were performed using three uniform grid sizes of 300 × 400, 350 × 450, and 400 × 500. The results of the grid and time-step sensitivity analyses are depicted in Fig. 2 in terms of the temperature time series (TTS) at monitoring point P_1 (0, 0.15), where the flow exhibits the strongest unsteady behavior. As shown in Fig. 2, the TTS obtained by means of different grid resolutions and time-step sizes are in outstanding agreement during the initial stage, exhibit only minor discrepancies throughout the transitional stage, and closely overlap in the fully developed stage (FDS).

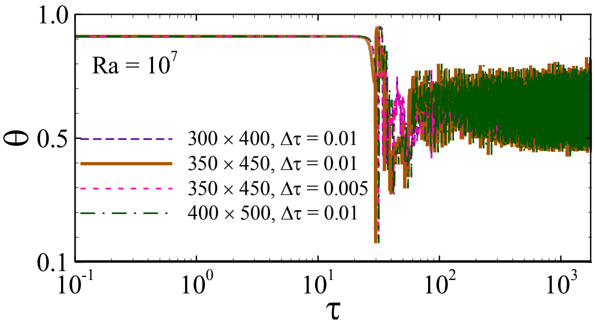

Fig. 2. Time series of temperature at point P_1 (0, 0.15) for Ra = 10^7 with different grids and time steps.

Table 2 presents the variation of average velocity at point P_1 (0, 0.15) in the FDS for different grid resolutions and time-step sizes. A maximum deviation of 0.82% is observed between the coarsest grid (300 × 400) and the finer grid (350 × 450) for a time step of 0.01. In contrast, the difference between the two finer grids (350 × 450) and (400 × 500) was minimal, at approximately 0.38%. Similarly, reducing the time step from 0.01 to 0.005 on the grid (350 × 450), the deviation is 0.27%. The results confirm that the numerical solution is essentially independent of the grid resolution considered, demonstrating that all tested meshes adequately resolve the flow. Therefore, considering the trade-off between computational efficiency and numerical accuracy, a grid resolution of (350 × 450) with a time step of 0.01 was selected for all subsequent simulations.

In this research, the normalized dissipative time scale was computed using the following equation [31]:

$$\lambda_k = \left(32\pi\sqrt{2}\right)^{1/4}\left(\frac{\text{Ra}}{\text{Pr}}\right)^{-3/8}. \tag{21}$$

Here, λ_k = 0.0169 for Ra = 10^7; so, the time steps of 0.005 and 0.01 are selected for the comparison.

Table 2. Variation of y-velocity at point P1 (0, 0.15) using different grids and time steps.

Grids and time steps	Average velocity	Variance
300 × 400 and Δτ = 0.01	0.0726	0.82%
350 × 450 and Δτ = 0.01	0.0732	-
350 × 450 and Δτ = 0.005	0.0734	0.27%
400 × 500 and Δτ = 0.01	0.07348	0.38%

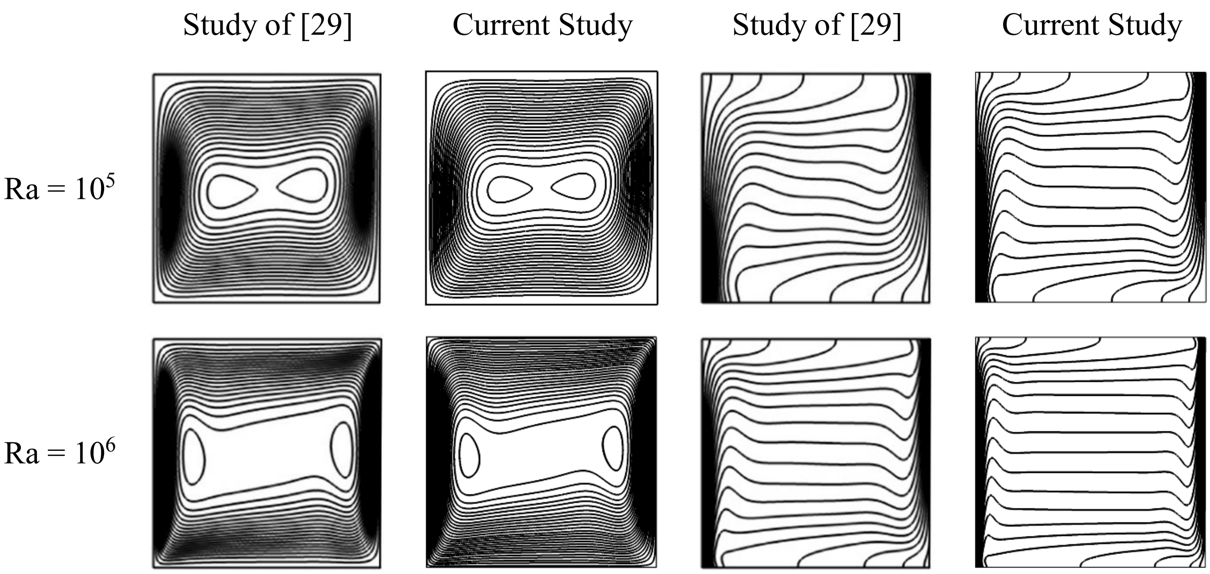

Fig. 3. Comparison of streamline and isotherm distributions obtained in the present study with those of Bawazeer and Alsoufi [29] for a square cavity at Pr = 1.0 and Ra = 10^5 and 10^6.

5- Model Validation

The precision and consistency of the current numerical model were qualitatively validated through comparison with the numerical results reported by Bawazeer and Alsoufi [29]. Their study examined NC in an unevenly heated square cavity, where the right and left vertical walls were maintained at cold and hot temperatures, respectively, while the horizontal walls were insulated. Under these boundary conditions, HT occurs solely through buoyancy-driven convection between the non-uniformly heated vertical walls, representing the classical NC problem inside a square cavity. The comparison was performed for Ra values of Ra = 10^5 and 10^6, with Pr = 1.0, as illustrated in Fig. 3. The results reveal outstanding agreement between the current results and those of Bawazeer and Alsoufi [29], thereby confirming the validity of the current numerical methodology. Furthermore, the model validated previously for a square cavity against the benchmark solutions of Basak et al. [41] (see also Hossain et al. [38] for additional details), providing further confidence in the accuracy of the present simulations.

6- Results and Discussion

The validated numerical methodology has been applied to examine NC, HT, and E_{gen} in a thermally stratified rectangular cavity, followed by a comparative assessment of thermal performance between rectangular and square geometries. The physical configuration consists of a uniformly heated bottom wall, a uniformly cooled top wall, and linearly thermally stratified vertical walls. A comprehensive set of 2D transient simulations was conducted over an extensive range of Ra, varying from 10 to 10^7, while maintaining a constant Pr of 7.01. As Ra rises, the flow undergoes a series of bifurcations, evolving from a symmetric, conduction-dominated state at low Ra to increasingly complex periodic and chaotic convection at higher Ra. The evolution of the flow structures, thermal fields, HT characteristics, and thermodynamic performance is systematically discussed in the following sections.

6- 1- Symmetric state

Figure 4 illustrates a 2D NC flow, featuring streamlines and isotherms to elucidate the reactions occurring within the enclosure. The cavity is subjected to a uniformly heated bottom wall, a uniformly cooled top wall, and linearly thermally stratified vertical sidewalls. These thermal boundary conditions promote the development of thermal boundary layers (TBL) along the enclosure surfaces, consisting of a heating TBL adjacent to the bottom wall and a cooling TBL near the top wall. The temperature gradients established within these boundary layers generate buoyancy forces that drive fluid circulation inside the cavity. The streamline and isotherm contours corresponding to Ra ranging from 10 to 10^4 are shown in Fig. 4. Throughout this Ra range, the flow retains a symmetric and predominantly conduction-dominated state, as illustrated in Figs. 4(a)-4(d). The isotherms remain nearly parallel and vertically oriented, indicating only minor distortion due to weak buoyancy effects. Consistent with the temperature field, the streamline patterns exhibit very weak and symmetric circulation, while no pronounced upward or downward thermal plumes are observed. These features demonstrate that buoyancy-induced convection is insufficient to overcome conductive heat transport at low Ra values, confirming that conduction remains the dominant HT mechanism within the enclosure.

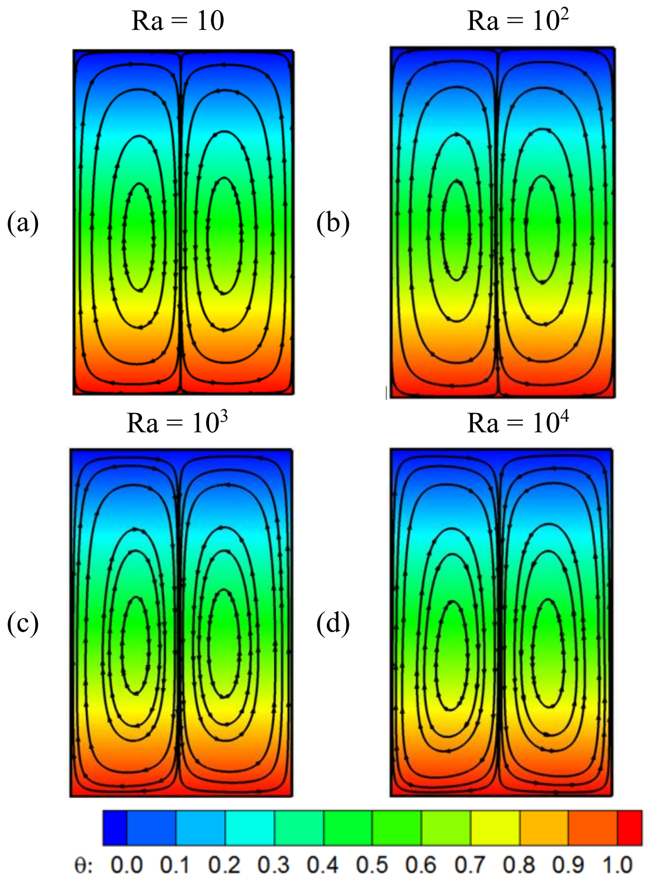

Fig. 4. Flow behavior for lower Ra at τ = 2000: (a) for Ra = 10, (b) for Ra = 10^2, (c) for Ra = 10^3, and (d) for Ra = 10^4.

6- 2- Asymmetric state

As the Ra exceeds a critical value, the stable symmetric flow becomes unstable and transitions to an asymmetric steady state. This transition is associated with a pitchfork bifurcation occurring at a critical Ra within the investigated range. At the initial stage (τ = 10), the flow remains symmetric with regard to the cavity's symmetric line for both Ra of 2 × 10^4 and 3 × 10^4, as shown in Fig. 5(a, b). However, as time progresses to (τ = 57), distinct differences emerge between the two cases. For Ra = 2 × 10^4, the flow retains its symmetric structure, as shown in Fig. 5(c), confirming the stability of the symmetric solution. In contrast, for Ra = 3 × 10^4, the primary convective cell shifts toward one side of the cavity, resulting in a clear breakdown of symmetry, as depicted in Fig. 5(d). The flow subsequently settles into a steady asymmetric state characterized by unequal circulation patterns on the two sides of the cavity.

These observations indicate that the critical Ra associated with the symmetry-breaking transition lies between 2 × 10^4 and 3 × 10^4. The emergence of asymmetry signifies the dominance of buoyancy-induced instabilities over the restoring mechanisms that maintain the symmetric flow configuration. It is important to note that the preference of the circulation cell for one side of the cavity does not reflect any inherent physical bias in the governing equations or numerical model. Rather, the selected asymmetric state is determined by infinitesimal perturbations arising from numerical round-off errors or initial disturbances. Consequently, an equally valid mirror-image solution would be obtained if the perturbation favored the opposite direction, which is a well-known feature of pitchfork bifurcations in symmetric convective systems.

To assess thermal non-uniformity caused by asymmetric flow patterns, the isotherm asymmetry in the cavity is computed using the subsequent formulation (refer to [39]):

$$I = \frac{\int [\theta(x,y) - \theta(-x,y)]^2 dx\, dy}{4\int [\theta(x,y)]^2 dx\, dy}\ . \tag{22}$$

The degree of asymmetry, denoted by I, serves as an indicator of flow symmetry. A value of I = 0 corresponds to a steady, symmetric state, whereas positive values of I reflect the onset of asymmetry. Figure 6 demonstrates the variation of I across a Ra range of 2 × 10^4 to 3 × 10^4. For the water-filled cavity, I remains nearly zero up to Ra = 2 × 10^4, confirming

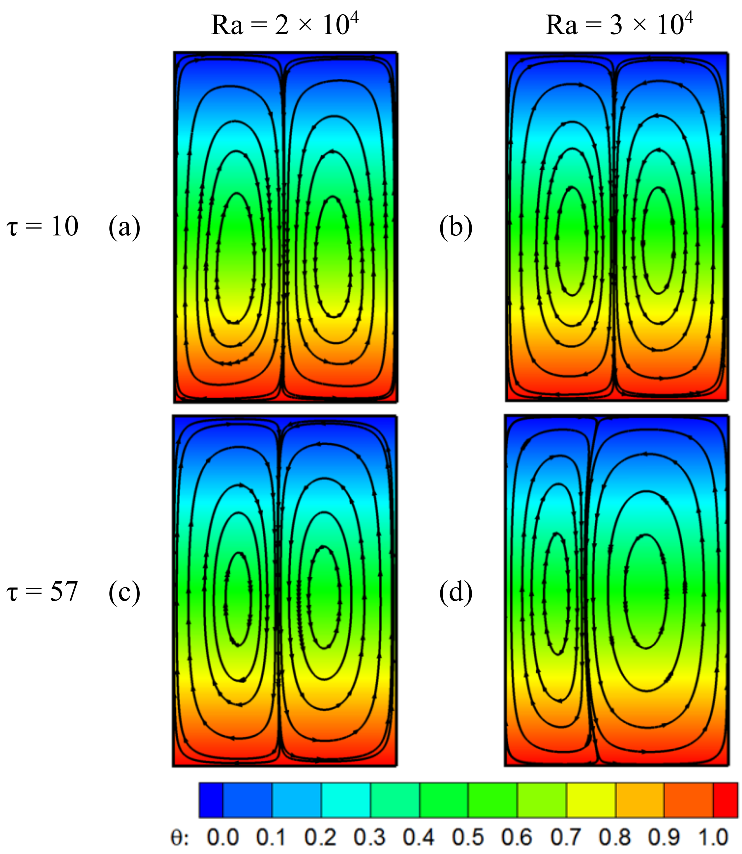

Fig. 5. Visualization of pitchfork bifurcation via isotherms and streamlines: (a, c) for Ra = 2 × 10^4, and (b, d) for Ra = 3 × 10^4.

the persistence of symmetry. At Ra = 3 × 10^4, however, I increases markedly, signaling the breakdown of symmetry and the emergence of an asymmetric flow regime, which we called a pitchfork bifurcation. Beyond this point, I continue to rise with increasing Ra, demonstrating the progressive strengthening of asymmetry under higher buoyancy forces. The authors' previous study in the square cavity [38] revealed that pitchfork bifurcation occurs between Ra = 8 × 10^3 and Ra = 10^4.

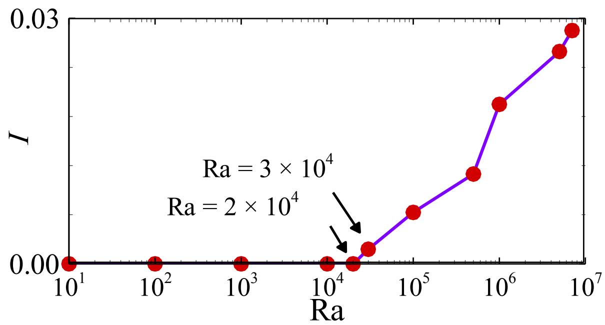

Fig. 6. Transition from a symmetrical to an asymmetrical state: correlation between Ra and the asymmetry index I in the cavity.

6- 3- Unsteady state

Figure 4 demonstrates that, at relatively low Ra values (10 to 10^4), the flow maintains symmetry with respect to the vertical centerline of the cavity. In this regime, buoyancy forces are insufficient to destabilize the symmetric circulation pattern, and the flow eventually reaches a symmetric steady state. As the Ra increases to 3 × 10^4, the symmetric solution loses stability, and an asymmetric flow structure emerges, as illustrated in Fig. 6. This symmetry-breaking transition is characteristic of a pitchfork bifurcation, marking the onset of an asymmetric convection regime. Further increasing the to 10^5, preserves the asymmetric nature of the flow, as shown in Fig. 7(a), at τ = 20 and at the FDS (τ = 2000) the convective cells increases and the flow becomes steady state, as depicted in Fig. 7(b).

A further increase in the Ra induces additional flow instabilities and promotes the transition to unsteady convection, as illustrated in Fig. 8. For both (Ra = 10^6 and Ra = 10^7), the flow structure becomes increasingly complex even at the early stage (τ = 10), characterized by stronger circulation and the formation of multiple convective cells,

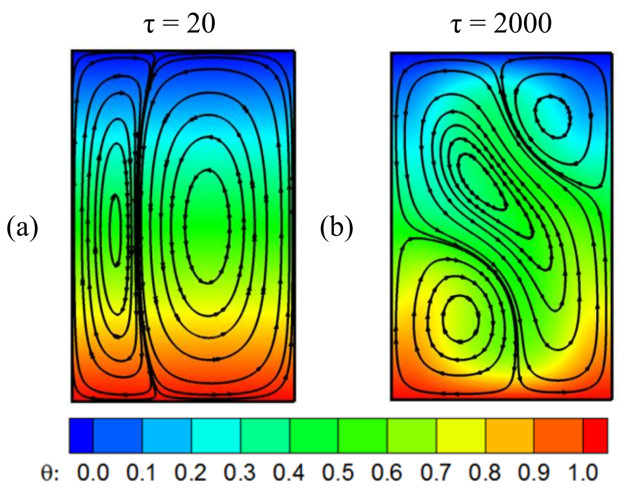

Fig. 7. Streamlines and isotherms illustrating flow development at Ra = 10^5: (a) remains asymmetric at τ = 20 and (b) becomes steady state at τ = 2000.

depicted in Fig. 8(a, b). At Ra = 10^6, the flow evolves into a periodic state at τ = 2000, as shown in Fig. 8(c). In this regime, the convective structures undergo regular oscillatory motion, indicating the emergence of time-dependent but deterministic behavior. The periodic oscillations arise from the increasing dominance of buoyancy-driven instabilities, which prevent the flow from reaching a stationary equilibrium.

When the Ra is further increased to 10^7, the flow undergoes a shift from periodic to chaotic convection. As illustrated in Fig. 8(d), the flow field becomes significantly more intricate, exhibiting irregular circulation patterns and enhanced interactions among multiple vortical structures. The isotherms display pronounced distortions and the appearance of small-scale thermal plumes, indicating intensified thermal mixing and loss of temporal regularity. These features are characteristic of chaotic convection, where the flow exhibits strong sensitivity to initial conditions and a broad spectrum of spatial and temporal scales. The progression from steady symmetric flow to asymmetric steady convection, followed by periodic oscillations and ultimately chaotic motion, highlights the rich sequence of bifurcations and dynamical transitions induced by increasing buoyancy forces within the cavity.

The shift from steady to chaotic flow is characterized using the TTS and power spectral density (PSD) at point P_2 (0, 0.40), as presented in Fig. 9. These analyses provide insight into the evolution of unsteady flow behavior at higher Ra. At Ra = 10^5, the TTS reaches a constant value after the initial transient period, indicating that the flow remains in a steady state at the FDS, as shown in Fig. 9(a). In contrast, the authors' previous study [38] reported a steady-state solution up to Ra = 2 × 10^5. As Ra increases, the flow undergoes a shift from a steady to a periodic state, indicating the occurrence of a Hopf bifurcation within the range 10^5 < Ra ≤ 2 × 10^5.

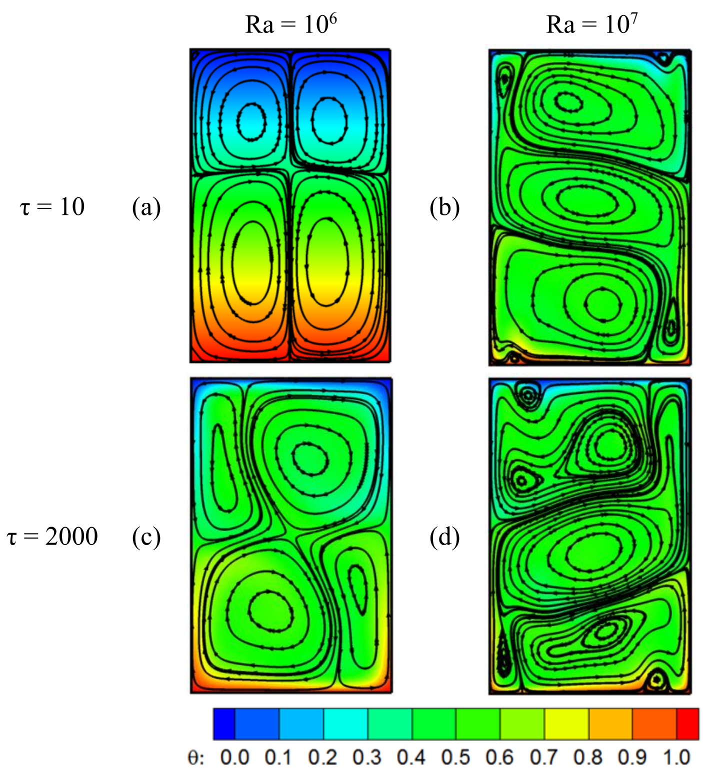

Fig. 8. Streamlines and isotherms illustrating unsteady flow development: (a, c) at Ra = 10^6, becomes periodic at τ = 2000 and (b, d) at Ra = 10^7, becomes chaotic at τ = 2000.

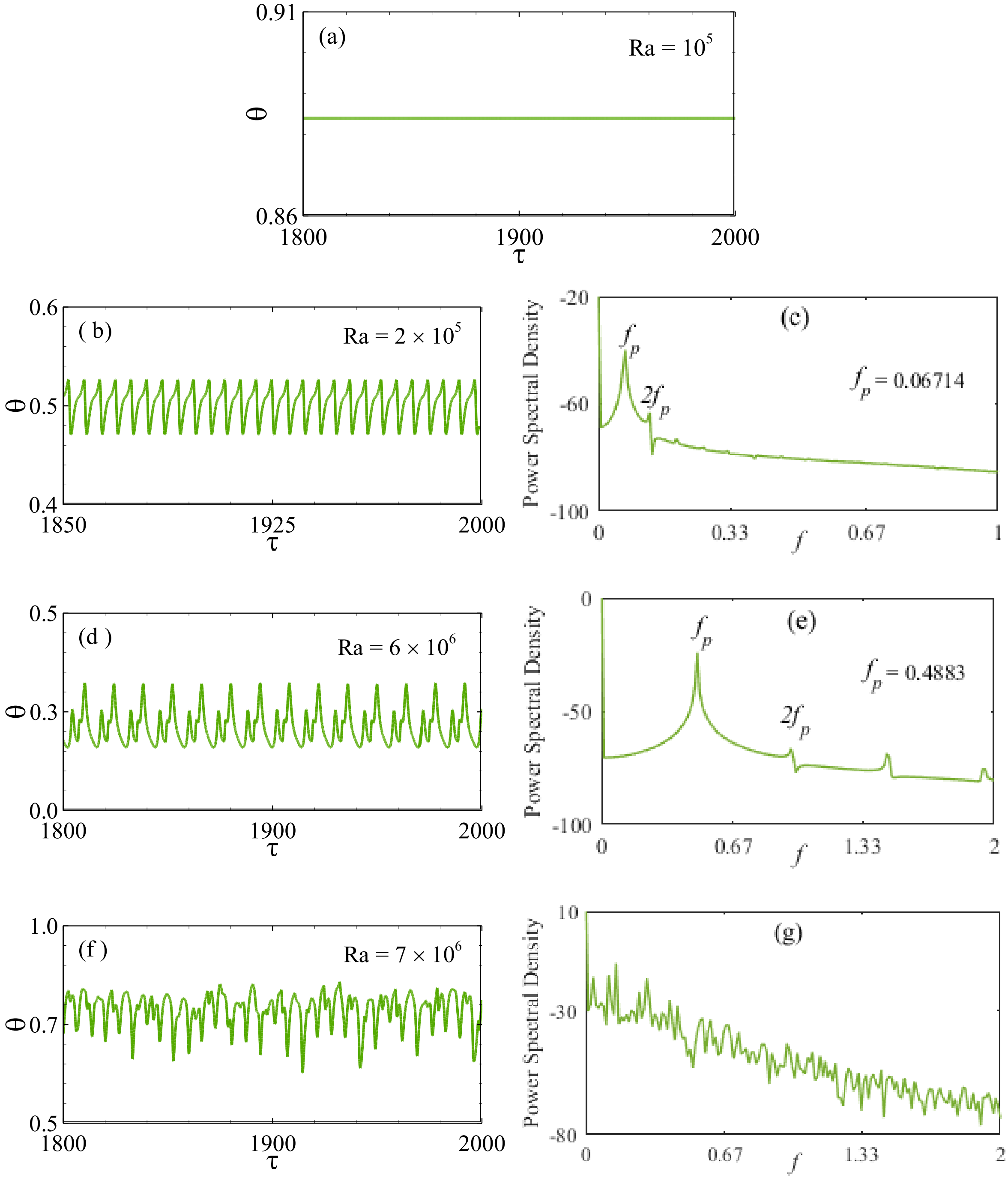

Fig. 9. Temperature time series and associated spectral analysis: (a) steady for Ra = 10^5; (b, c) shifting to periodic flow for Ra = 2 × 10^5; (d, e) continued periodic for Ra = 5 × 10^6; and (f, g) changeover to chaotic at Ra = 7 × 10^6.

Beyond this critical threshold, periodic oscillations persist over a range of Ra, from Ra = 2 × 10^5 to 6 × 10^6. The periodic nature of the flow is confirmed by the corresponding PSD spectra shown in Figs. 9(c) and 9(e), which exhibit distinct dominant peaks at the fundamental frequencies of f_p = 0.06714 and 0.4883 for Ra = 2 × 10^5 and 6 × 10^6, respectively. The presence of a single dominant frequency and its harmonics is characteristic of periodic flow behavior. A further increase in Ra to Ra = 7 × 10^6 leads to a qualitative change in the flow dynamics. The regular oscillatory pattern observed in the TTS is replaced by irregular fluctuations, as illustrated in Fig. 9(f), indicating the emergence of chaotic flow. This transition is further supported by the PSD spectrum in Fig. 9(g), where the dominant fundamental peak frequency diminishes and confirms the beginning of chaotic flow. However, [38] identified the Hopf bifurcation within the range 3 × 10^5 ≤

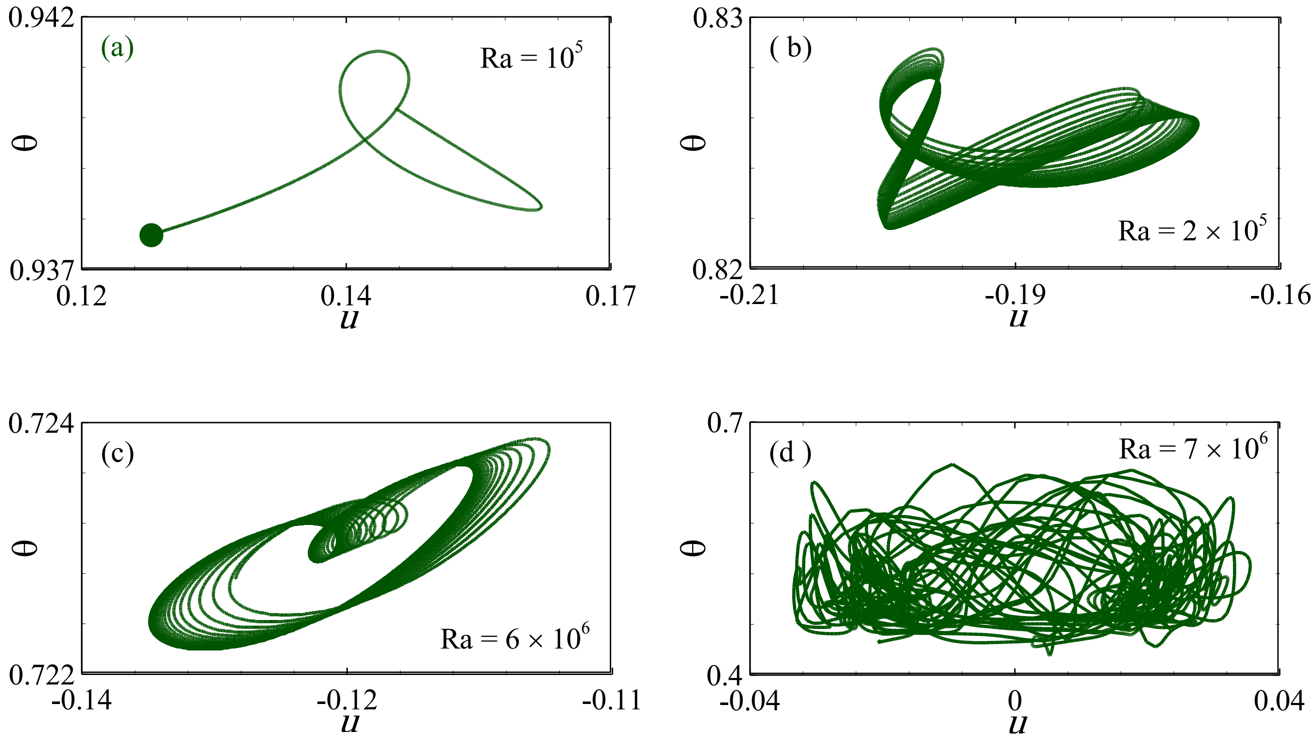

Fig. 10. Limit point and limit cycles at point P_3 (-0.30, 0.20): (a) for Ra = 10^5, (b) for Ra = 2×10^5, (c) for Ra = 5×10^6, and (d) for Ra = 7×10^6.

Ra ≤ 10^6, whereas chaotic behavior emerged at Ra = 2×10^6.

To further characterize the flow dynamics, the phase space trajectories in the u-θ plane at point P_3 (-0.30, 0.20) are analyzed over the time interval τ =1000 to 2000, as shown in Fig. 10. The evolution of the phase-space trajectories provides valuable insight into the sequence of dynamical transitions occurring with increasing Ra. At Ra = 10^5, the trajectory converges to a single fixed point (Fig. 10(a)), indicating that the system reaches a stable steady state after the initial transient period. As the Ra increases to Ra = 2 × 10^5, the fixed point loses stability, and a closed-loop trajectory emerges (Fig. 10(b)). The appearance of this stable limit cycle signifies the emergence of a Hopf bifurcation and confirms the shift from steady to periodic flow. Further increasing the Ra to Ra = 5 × 10^6 preserves the closed-loop structure of the phase portrait (Fig. 10(c)), demonstrating that the flow remains periodic despite the increased oscillation intensity. A qualitative change in the system dynamics is observed at Ra = 7 × 10^6. As shown in Fig. 10(d), the phase trajectory becomes irregular and non-repeating, occupying a broader region of the phase space. Such behavior is characteristic of a chaotic attractor and indicates the breakdown of periodicity. The resulting phase portrait confirms the changeover from periodic to chaotic flow, consistent with the TTS and PSD analyses presented previously.

7- Entropy Generation

Table 3 presents a comparison of the variations in E_{avg} and Be_{avg} for square and rectangular enclosures at different Ra values. For both geometries, the E_{gen} increases significantly with increasing Ra, whereas Be_{avg} exhibits a decreasing trend. Under these conditions, the fluid velocity and the associated E_{avg} are primarily influenced by the thermal transport mechanism, which is dominated by conductive HT at lower Ra. As Ra rises, buoyancy-driven convection becomes more pronounced, leading to enhanced fluid circulation and consequently, a rise in E_{avg}. The authors' previous investigation [38] revealed that, for a square cavity, the E_l contours closely align with those of E_{avg} due to HT up to Ra = 10^5. This suggests that the contribution of E_{gen} associated with FF remains negligible within this range, confirming that the flow irreversibility is predominantly governed by HT induced mechanism.

A significant variation is observed at higher Ra, specifically at Ra = 10^6, as presented in Table 3. At this higher Ra value, frictional effects become dominant, and the local E_{avg} contours exhibit a close resemblance to those induced by FF. The contribution of FF to the total E_{gen} increases relative to that of HT, primarily due to the intensified viscous dissipation associated with stronger convective motion at high Ra. At Ra = 10^6, the E_{avg} in the square cavity is 57.96, while in the rectangular cavity it is 47.57. When Ra rises to

Table 3. Comparison of Eavg and Beavg between square and rectangular cavities for different Ra.

Ra	Square cavity		Rectangular cavity	
	E_{avg}	Be_{avg}	E_{avg}	Be_{avg}
10^4	4.96	0.999	3.76	0.999
10^5	18.47	0.954	12.96	0.972
10^6	57.96	0.453	47.57	0.480
5×10^6	131.95	0.147	132.74	0.175
7×10^6	344.45	0.069	349.31	0.106

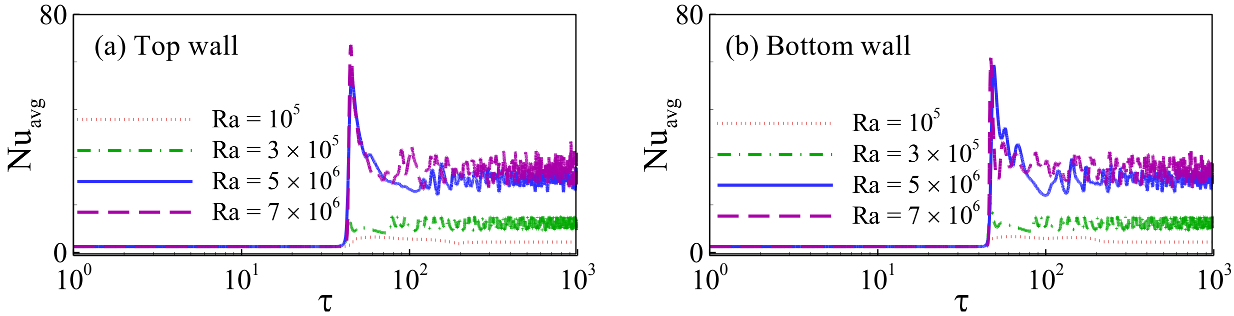

Fig. 11. Nuavg time series for different Ra: (a) at the top wall and (b) at the bottom wall.

5×10^6, the E_{avg} values increase to 131.95 and 132.74 for the square and rectangular cavities, respectively. The comparison reveals that for Ra = 10^4 to 10^6, the E_{avg} of the square cavity exceeds that of the rectangular cavity. However, at higher Ra values (5×10^6 and 7×10^6), the rectangular configuration exhibits slightly higher E_{avg}, reflecting the enhanced role of frictional irreversibility under strong convective regimes.

An evident negative correlation is observed between Be_{avg} and Ra, with Be_{avg} consistently diminishing as Ra rises. The square enclosure generally exhibits slightly lower Be_{avg} values compared to the rectangular configuration. The extreme value of Be_{avg} ($Be_{avg,\ max} \approx 1$) occurs when E_{avg} is primarily influenced by HT induced irreversibilities. This suggests that, at lower Ra, thermal diffusion is the primary mechanism driving E_{gen}. As Ra rises, the gradual decline in Be_{avg} signifies the growing contribution of FF irreversibilities to the total E_{avg}, consequently reducing the relative importance of HT related effects. Specifically, at Ra = 10^5, Be_{avg} is 0.954 in the square cavity and 0.972 in the rectangular cavity. When Ra rises to 10^6, Be_{avg} decreases to 0.453 and 0.480 for the square and rectangular cavities, respectively. These results show that, within the square enclosure, the influence of FF irreversibility is more pronounced.

8- Heat Transfer

Although the streamline and isotherm distributions do not provide a direct quantitative measure of the heat transfer rate at the cavity boundaries, they offer important qualitative insight into the underlying flow structures and thermal transport mechanisms. Figure 11 presents the temporal evolution of the average Nusselt number (Nu_{avg}) at the heated bottom and cooled top walls of the rectangular cavity. Owing to the initially thermally stratified fluid, the temperature adjacent to each boundary is closely equivalent to the local wall temperature, including the uniformly heated bottom wall, the uniformly cooled top wall, and the linearly stratified vertical walls. As a result, the initial temperature gradients at the heated and cooled boundaries are relatively weak, leading to low Nu_{avg} values and conduction-dominated HT during the early stage of the transient process. With increasing Ra, buoyancy effects become progressively stronger, promoting convective motion and enhancing HT. Consequently, temporal fluctuations in Nu_{avg} emerge and increase in amplitude as the flow evolves from a steady to an unsteady state. In the FDS, the temporal response of Nu_{avg} reflects the underlying flow regime. Specifically, Nu_{avg} remains constant for Ra ≤ 10^5, indicating a steady-state flow. At Ra = 3×10^5,

Table 4. Variation of Nuavg at the bottom wall for different cavity geometries.

Ra	Rectangular cavity	Square cavity
10^4	2.00	2.00
10^5	3.67	5.79
10^6	15.5	13.44
5×10^6	24.97	20.96
7×10^6	27.55	26.24

Table 5. Comparison of Nuavg over all cavity walls for the rectangular and square cavity configurations over different Ra.

Ra	Rectangular cavity	Square cavity
10^4	1.37	1.53
10^5	3.76	5.34
10^6	9.37	10.64
5×10^6	15.29	13.41
7×10^6	17.06	15.83

periodic oscillations appear, signifying the onset of time-periodic convection following a Hopf bifurcation. As the Ra increases further to Ra $\geq 7 \times 10^6$, the periodic behavior transitions into irregular, chaotic oscillations, reflecting the development of chaotic convection. The observed behavior corresponds closely with the bifurcations and flow dynamics portrayed in Figs. 9 and 10.

9- Influence of Square and Rectangular Geometries on Heat Transfer

Table 4 presents the variation of Nu_{avg} at the bottom wall for rectangular and square cavities over a range of Ra. The Nu_{avg} values for the square cavity are taken from the authors' previous study [38] to facilitate a direct comparison of the influence of cavity geometry on HT performance. At Ra = 10^4, both configurations exhibit an identical Nu_{avg} value of 2.00, which reflects that HT at the bottom is predominantly governed by conduction, as buoyancy-induced circulation remains weak. As Ra rises to 10^5, buoyancy effects become more pronounced, and convective transport starts to contribute significantly. In this regime, the square cavity exhibits a higher Nu_{avg} of 5.79 compared with 3.67 for the rectangular cavity, indicating that the square geometry promotes the earlier development of convective circulation. This behavior suggests that the shorter vertical dimension and symmetric configuration of the square cavity facilitate the formation of stronger thermal plumes, thereby increasing the HT rate from the heated bottom wall. A different trend is observed at higher Ra values. At Ra = 10^6, the rectangular cavity exhibits a larger Nu_{avg} (15.50) than the square cavity (13.44), indicating that the elongated geometry becomes more favorable for convective HT as buoyancy forces intensify. The enhanced performance of the rectangular cavity persists at Ra = 5×10^6 and 7×10^6, where the Nu_{avg} values increase to 24.97 and 27.55, respectively, compared with 20.96 and 26.24 for the square cavity. Although the difference becomes relatively small at Ra = 7×10^6, the rectangular cavity consistently maintains a higher HT rate. This marginal enhancement in the rectangular cavity reflects the effect of its geometry configuration, which promotes stronger circulation loops and more efficient thermal mixing near the bottom surface.

Table 5 compares the Nu_{avg} at all cavity walls for the rectangular and square cavity configurations over a range of Ra. The results demonstrate that both Ra and cavity geometry play significant roles in determining the HT characteristics. At Ra = 10^4, both cavity configurations exhibit relatively low Nu_{avg} values of 1.37 and 1.53 for the rectangular and square cavities, respectively. In this regime, temperature gradients drive heat transport through molecular diffusion rather than convective motion. With increasing Ra to 10^5, the influence of buoyancy becomes more pronounced, resulting in a considerable enhancement of convective HT. The square cavity exhibits a significantly larger Nu_{avg} of 5.34 compared with 3.76 for the rectangular cavity, suggesting that the square geometry promotes a more rapid establishment of NC. This enhancement is attributed to the symmetric enclosure,

Table 6. Variation of ECOP within the cavities for different Ra.

Ra	ECOP in rectangular cavity	ECOP in square cavity
10^4	0.3643617	0.3084677
10^5	0.2901235	0.2891175
10^6	0.1969729	0.1835749
5×10^6	0.1151876	0.1016294
7×10^6	0.0488391	0.0459573

which facilitates the development of stronger thermal plumes and more efficient circulation within the cavity. At Ra = 10^6, both cavities exhibit well-established buoyancy-driven convection, leading to a further increase in Nu_{avg}. The square cavity attains Nu_{avg} = 10.64, while the rectangular cavity records Nu_{avg} = 9.37. This observation indicates that the square cavity maintains a more effective HT mechanism during the intermediate convection regime. However, at Ra = 5×10^6 and 5×10^6, the trend reverses: the rectangular cavity surpasses the square cavity. The comparison shows that for higher Ra, the Nu_{avg} value of a square cavity is lower than that of a rectangular cavity. Quantitatively, the HT rate in the rectangular cavity is approximately 7.21% higher than that in the square cavity at Ra = 7×10^6. The Nu_{avg} for the rectangular cavity is approximately 7.21% higher than that of the square cavity. This enhancement suggests that the elongated geometry of the rectangular cavity supports stronger circulation cells and more effective thermal mixing under high-buoyancy conditions, thereby enhancing convective HT at the walls.

10- Thermal Performance Evaluation

The ecological coefficient of performance (ECOP) defined in Eq. (22), representing the system's ecological efficiency, can be formulated as follows (refer to [37]):

$$\mathrm{ECOP} = \frac{\mathrm{Nu}_{avg}}{E_{avg}}. \tag{23}$$

The ECOP is employed to evaluate the overall thermodynamic performance of the computational domain by simultaneously accounting for HT enhancement and average E_{gen}. A higher ECOP value indicates superior thermal performance, as it reflects a lower rate of average E_{gen} and, consequently, reduced thermodynamic irreversibility. In contrast, a lower ECOP value signifies increased entropy production resulting from intensified convective transport and associated irreversible processes, leading to a reduction in the overall thermodynamic efficiency of the system.

Table 6 illustrates the variation of the ECOP for the rectangular and square cavity configurations over a range of Ra. At lower Ra values (Ra = 10^4 to 10^5), both cavities exhibit relatively high ECOP values, indicating that average E_{gen} remains comparatively low under conduction-dominated conditions. The rectangular cavity consistently achieves a slightly higher ECOP than the square cavity, with values of 0.3643617 and 0.2901235 compared with 0.3084677 and 0.2891175, respectively. The difference is particularly significant at Ra = 10^4, where the rectangular cavity exhibits approximately 18.1% higher ECOP than the square cavity, reflecting its superior thermodynamic efficiency in the low Ra regime. As the Ra increases, the ECOP decreases progressively for both cavity geometries. At Ra = 10^6, the ECOP reduces to 0.1969729 for the rectangular cavity and 0.1835749 for the square cavity, indicating that stronger buoyancy-induced convection is accompanied by increased entropy generation and greater thermodynamic irreversibility.

A further increase in the Ra to 5×10^6 and 7×10^6 results in a pronounced reduction in ECOP, with values of 0.1151876 and 0.0488391 for the rectangular cavity, compared with 0.1016294 and 0.0459573 for the square cavity, respectively. This decline reflects the increasing dominance of irreversible thermal transport processes as convective motion intensifies. Throughout the investigated Ra range, the rectangular cavity consistently maintains a higher ECOP than the square cavity, demonstrating its superior thermodynamic performance. At Ra = 5×10^6, the ECOP of the rectangular cavity is approximately 13.3% higher than that of the square cavity, while at Ra = 7×10^6, the improvement remains about 6.3%. These findings indicate that, although increasing the Ra enhances convective HT, it also accelerates average E_{gen}, leading to a reduction in overall thermodynamic efficiency. Consequently, both cavity configurations experience a deterioration in ECOP with increasing Ra; however, the rectangular cavity consistently provides better thermal performance by maintaining lower thermodynamic irreversibility over the entire range of operating conditions.

11- Conclusions

A detailed numerical investigation has been carried out to examine the influence of Ra on NC and E_{gen} in a thermally stratified rectangular cavity, followed by a comparative assessment of thermal performance between rectangular and square geometries. The enclosure configuration comprises a uniformly heated bottom wall, linearly stratified vertical walls, and a cooled top wall. The FV method was employed for the numerical simulations, considering a Pr of 7.01 and a broad array of Ra = 10 to 10^7.

The results revealed that, in the rectangular cavity, multiple bifurcations occur in the changeover from the symmetric to the chaotic state. Specifically:

- The symmetry-breaking (pitchfork) bifurcation occurred between Ra = 2×10^4 and Ra = 3×10^4.
- The onset of periodic oscillations (Hopf bifurcation) occurred between the range of Ra = 10^5 and Ra = 2×10^5.
- The changeover from periodic to chaotic flow was observed between Ra = 6×10^6 and Ra = 7×10^6.

The mechanisms of E_{gen} were further investigated for both cavities by considering the total E_{gen} due to HT and FF irreversibilities by means of the $Be_{avg.}$ values.

- At lower Ra **(**$\leq 10^5$**)**, entropy production was dominated by HT irreversibility, with negligible FF.
- At higher Ra **(**$\geq 10^6$**)**, FF played a major role in the overall entropy production due to the intensified buoyancy-driven flow, leading to higher E_{gen}.

The comparison of thermal performance demonstrated that cavity geometry has a significant influence on convective HT under convection-dominated conditions. At Ra = 7×10^6, the rectangular cavity achieved a HT rate approximately 7.21% higher than that of the square cavity, indicating its superior capability to sustain stronger circulation and more effective thermal mixing. Evaluation of the ECOP further confirmed the thermodynamic advantage of the rectangular configuration. Although ECOP decreased with increasing Ra for both geometries because of enhanced entropy production, the rectangular cavity consistently maintained higher values throughout the investigated range. At Ra = 7×10^6, the ECOP of the rectangular cavity was approximately 6.3% higher than that of the square cavity, demonstrating its superior overall thermodynamic performance.

The findings indicate that with the increase of Ra values, HT rates and average E_{gen} increase for both cavities. However, in terms of thermal performance, the rectangular cavity demonstrates superior efficiency relative to the square geometry. These results contribute to the optimization of cavity designs in thermal engineering applications, emphasizing the critical balance between HT enhancement and energy efficiency.

Declaration of generative AI and AI-assisted technologies in the manuscript preparation process

During the preparation of this manuscript, the authors used ChatGPT to assist with improving grammar and enhancing the clarity and quality of the English language. All AI-assisted text was subsequently reviewed, revised, and edited by the authors to ensure its accuracy and appropriateness. The authors are solely responsible for the content, interpretation, and conclusions presented in the final published version of the manuscript.

Nomenclature

Be_l	local Bejan number
Be_{avg}	average Bejan number
Cp	specific heat (J/kg.K)
E_{avg}	average entropy generation
E_{ff}	entropy generation due to fluid friction
E_{gen}	entropy generation
E_{ht}	entropy generation due to heat transfer
E_l	local entropy generation
g	gravitational force (m/s^2)
H	length and height of the cavity (m)
k	thermal conductivity (W/(m·K))
Nu	Nusselt number
Nu_{avg}	average Nusselt number
P	pressure (N/m^2)
p	dimensionless pressure
Pr	Prandtl number
Ra	Rayleigh number, $g\beta(T_h - T_c)H^3/\nu\kappa$
t	time (s)
T	temperature (K)
T_c	temperature of the top wall (K)
T_h	temperature of the bottom wall (K)
T_i	temperature of the inclined walls (K)
T_∞	environmental temperature (K)
U, V	velocity components (m/s)
u, v	dimensionless velocity components
X, Y	coordinates
x, y	dimensionless coordinates
Greek symbols	
α	thermal diffusivity (m^2/s)
θ	dimensionless temperature
ν	kinematic viscosity (m^2/s)
ψ	irreversibility distribution ratio
ρ	density (kg/m^3)
τ	dimensionless time
$\Delta\tau$	dimensionless time step
θ_c	dimensionless temperature of the top wall
θ_h	dimensionless temperature of the bottom wall
θ_i	dimensionless temperature of the vertical walls

References

[1] T.L. Bergman, Fundamentals of heat and mass transfer. John Wiley & Sons, 2011.

[2] A. Bejan, Convection heat transfer. John Wiley & Sons, 2013.

[3] M.M. Rahman, M.A. Hye, M.M. Rahman, M.M. Rahaman, Numerical simulation of MHD free convection mass and heat transfer fluid flow over a vertical porous plate in a rotating system with an induced magnetic field. Annals of Pure and Applied Mathematics, 7(2) (2014) 35-44.

[4] M.A. Kawser, M.M. Rahaman, Exact travelling wave solutions of the Jeffery-Hamel flow of a non-Newtonian fluid using sine-cosine method, J. Math. Comput. Sci., 14, (2024) Article-ID 3.

[5] A. Zoubir, R. El Otmani, R. Bouferra, L. Essaleh, Effects of thermal stratification on natural convection in a symmetrically heated channel: Comparison of characteristic quantities between air and water, Case Studies in Thermal Engineering, 45 (2023) 102950.

[6] M.M. Rahaman, R. Titab, S. Bhowmick, R.N. Mondal, S.C. Saha, Unsteady 2D flow in an initially stratified air-filled trapezoid, Jagannath Univ. J. Sci., 8 (2022) 1-6.

[7] M.M. Rahaman, S. Bhowmick, R.N. Mondal, S.C. Saha. Unsteady natural convection in an initially stratified air-filled trapezoidal enclosure heated from below, Processes, 10(7) (2022) 1383.

[8] M.M. Rahaman, S. Bhowmick, B.P. Ghosh, F. Xu, R.N. Mondal, S.C. Saha, Transient natural convection flows and heat transfer in a thermally stratified air-filled trapezoidal cavity, Thermal Science and Engineering Progress, 47 (2024) 102377.

[9] M. Bouafia, O. Daube, Natural convection for large temperature gradients around a square solid body within a rectangular cavity, International Journal of Heat and Mass Transfer, 50(17-18) (2007) 3599-3615.

[10] M.M. Rahaman, S. Bhowmick, S.C. Saha, R.N. Mondal, Unsteady natural convection flow of two-phase fluids within a V-shaped cavity. AIP Conference Proceedings, 3451(1), (2026), 070002.

[11] H. Karatas, T. Derbentli, Natural convection in differentially heated rectangular cavities with time-periodic boundary condition on one side, International Journal of Heat and Mass Transfer, 129 (2019) 224-237.

[12] N.A.G. Charles, A.K. Otieno, K. M. Stephen, Turbulent Natural Convection in A Rectangular Enclosure, German Journal of Advanced Scientific Research, 3(3) (2020) 73-73.

[13] V.S. Berdnikov, V.A. Grishkov, N.A. Shumilov, Development of unsteady convection in a rectangular cavity with sudden heating of a vertical wall, Thermophysics and Aeromechanics, 27(4) (2020) 529-537.

[14] A. Fichera, M. Marcoux, A. Pagano, R Volpe, An analytical model for natural convection in a rectangular enclosure with differentially heated vertical walls, Energies, 13(12) (2020) 3220.

[15] S.D. Farahani, A.D. Farahani, H.F. Öztop, Natural convection in a rectangular tall cavity in the presence of an oscillating and rotating cylinder, Colloids and Surfaces A: Physicochemical and Engineering Aspects, 647 (2022) 129027.

[16] Z. Begum, M. Saleem, S.U. Islam, S. C. Saha, Numerical study of natural convection flow in rectangular cavity with viscous dissipation and internal heat generation for different aspect ratios, Energies, 16(14) (2023) 5267.

[17] G. de Vahl Davis, Natural convection of air in a square cavity: a benchmark numerical solution, International Journal for Numerical Methods in Fluids, 3(3) (1983) 249-264.

[18] T. Pesso, S. Piva, Laminar natural convection in a square cavity: low Prandtl numbers and large density differences, International Journal of Heat and Mass Transfer, 52(3-4) (2009) 1036-1043.

[19] A.A. Hakeem, S. Saravanan, P. Kandaswamy, Natural convection in a square cavity due to thermally active plates for different boundary conditions, Computers & Mathematics with Applications, 62(1) (2011) 491-496.

[20] S.K. Choi, S.O. Kim, Comparative analysis of thermal models in the lattice Boltzmann method for the simulation of natural convection in a square cavity, Numerical Heat Transfer, Part B: Fundamentals, 60(2) (2011) 135-145.

[21] C. Butler, D. Newport, M. Geron, Natural convection experiments on a heated horizontal cylinder in a differentially heated square cavity, Experimental Thermal and Fluid Science, 44 (2013) 199-208.

[22] S. Saravanan, Natural convection in square cavity with heat-generating baffles, Applied Mathematics and Computation, 244 (2014) 1-9.

[23] I. Kouroudis, P. Saliakellis, S.G. Yiantsios, Direct numerical simulation of natural convection in a square cavity with uniform heat fluxes at the vertical sides: Flow structure and transition, International Journal of Heat and Mass Transfer, 115 (2017) 428-438.

[24] L. El Moutaouakil, M. Boukendil, Z. Zrikem, A. Abdelbaki, Natural convection and surface radiation heat transfer in a square cavity with an inner wavy body, International Journal of Thermophysics, 41(8) (2020) 109.

[25] Z. Wang, T. Wang, G. Xi, Z. Huang, Periodic unsteady natural convection in square enclosure induced by inner circular cylinder with different vertical locations, International Communications in Heat and Mass Transfer, 124 (2021)105250.

[26] O. Oyewola, S. Afolabi, O. Ismail, M. Olasinde, Convective heat transfer in a square cavity with embedded circular heated block at different positions, Frontiers in Heat and Mass Transfer, 18(1) (2022) 1-7.

[27] H.M. El, Z. Lafdaili, Turbulent natural-convection heat transfer in a square cavity with nanofluids in the presence of an inclined magnetic field, Thermal Science, 26(4 Part A) (2022) 3201-3213.

[28] F. Zemani, A Sabeur, O. Ladjedel, A. Chelih, Natural convective heat transfer in a square cavity with a curved hot wall partially heated from below, Physics of Fluids, 37(1) (2025) 019101.

[29] S.A. Bawazeer, M.S. Alsoufi, Natural convection in a square Cavity: Effects of Rayleigh and Prandtl numbers on heat transfer and flow patterns, Case Studies in Thermal Engineering, 73 (2025) 106680.

[30] S.M. Shavik, M.N. Hassan, A.M. Morshed, M.Q. Islam, Natural convection and entropy generation in a square inclined cavity with differentially heated vertical walls, Procedia Engineering, 90 (2014) 557-562.

[31] G.G. Ilis, M. Mobedi, B. Sunden, Effect of aspect ratio on entropy generation in a rectangular cavity with differentially heated vertical walls, International Communications in Heat and Mass Transfer, 35(6) (2008) 696-703.

[32] S.Z. Shuja, B.S. Yilbas, M.O. Budair, Natural convection in a square cavity with a heat-generating body: entropy consideration, Heat and Mass Transfer, 36(4) (2000) 343-350.

[33] A.K. Hussein, K. Lioua, R. Chand, S. Sivasankaran, R. Nikbakhti, D. Li, B.M. Naceur, B.A. Habib, Three-dimensional unsteady natural convection and entropy generation in an inclined cubical trapezoidal cavity with an isothermal bottom wall, Alexandria Engineering Journal, 55(2), (2016) 741-755.

[34] M.M. Rahaman, S. Bhowmick, G. Saha, F. Xu, S.C. Saha, Transition to chaotic flow, bifurcation, and entropy generation analysis inside a stratified trapezoidal enclosure for varying aspect ratio, Chinese Journal of Physics, 91 (2024) 867-882.

[35] D. Charreh, S.U. Islam, S. Talib, M. Saleem, M.A. Abbas, S. Ahmad, Numerical investigation of entropy generation and Magnetohydronamic natural convection in a porous square cavity with four embedded cylinders, Heliyon, 10(13) (2024) e33897.

[36] M.M. Rahaman, S. Bhowmick, S.C. Saha, Thermal performance and entropy generation of unsteady natural convection in a trapezoid-shaped cavity, Processes, 13(3) (2025) 921.

[37] M.M. Rahaman, S. Bhowmick, S.C. Saha, Unsteady Natural Convection and Entropy Generation in Thermally Stratified Trapezoidal Cavities: A Comparative Study, Processes, 13(6) (2025) 1908.

[38] M.N. Hossain, S.M.H. Shaon, M.M. Rahaman, Transient Natural Convection and Entropy Generation Analysis in a Stratified Square Enclosure, AUT Journal of Mechanical Engineering, 10(2) (2025) 153-166.

[39] M.M. Rahaman, S. Bhowmick, R.N. Mondal, S.C. Saha, A computational study of chaotic flow and heat transfer within a trapezoidal cavity, Energies, 16(13) (2023) 5031.

[40] S. Bhowmick, F. Xu, M.M. Molla, S.C. Saha, Chaotic phenomena of natural convection for water in a V-shaped enclosure, International Journal of Thermal Sciences, 176 (2022) 107526.

[41] T. Basak, S. Roy, A.R. Balakrishnan, Effects of thermal boundary conditions on natural convection flows within a square cavity, International Journal of Heat and Mass Transfer, 49(23-24) (2006) 4525-4535.

[42] S.M.H. Shaon, M.M. Rahaman, Unsteady natural convection and heat transfer analysis within a thermally stratified air-filled square enclosure, Mathematics and Mechanics of Complex Systems, 14(1) (2025) 37-57.

[43] S.S.M. Hassan, S. Khan, M.M. Rahaman, S, Bhowmick, S.C. Saha, Unsteady Natural Convection Flow within a Thermally Stratified Air-Filled Rectangular Cavity, Available at SSRN 6201198 (2026).

[44] S.S.M. Hassan, M.M. Rahaman, S.C. Saha, S. Bhowmick, Comparative Analysis of Unsteady Natural Convection and Thermal Performance in Rectangular and Square Cavities Filled with Stratified Air, Fluids, 11(2) (2026) 33.

HOW TO CITE THIS ARTICLE

Md. N. Hossain, S. M. Hassan Shaon, Md. M. Rahaman, Transient Natural Convection and Thermal Performance Analysis in Stratified Water-Filled Rectangular and Square Cavities: A Comparative Study, AUT J. Model. Simul., 58(1) (2026) 95-112.

DOI: 10.22060/miscj.2026.24965.5445